Quasiparticle Interference on Cubic Perovskite Oxide Surfaces

Yoshinori Okada, Shiue-Yuan Shiau, Tay-Rong Chang, Guoqing Chang, Masaki Kobayashi, Ryota Shimizu, Horng-Tay Jeng, Susumu Shiraki, Hiroshi Kumigashira, Arun Bansil, Hsin Lin, and Taro Hitosugi

Phys. Rev. Lett. **119**, 086801 — Published 22 August 2017

DOI: 10.1103/PhysRevLett.119.086801

Quasiparticle interference on cubic perovskite oxide surfaces

Yoshinori Okada[1,*], Shiue-Yuan Shiau[2,3], Tay-Rong Chang[4,5], Guoqing Chang[2,3], Masaki Kobayashi[6], Ryota Shimizu[1], Horng-Tay Jeng[4, 7], Susumu Shiraki[1], Hiroshi Kumigashira[6], Arun Bansil[8], Hsin Lin[2,3], Taro Hitosugi[1, 9]

[1] Advanced Institute for Materials Research (AIMR), Tohoku University, Sendai 980-8577, Japan

[2] Centre for Advanced 2D Materials and Graphene Research Centre, National University of Singapore, Singapore 117546

[3] Department of Physics, National University of Singapore, Singapore 117542

[4] Department of Physics, National Tsing Hua University, Hsinchu 30013, Taiwan

[5] Department of Physics, National Cheng Kung University, Tainan, 701, Taiwan

[6] Photon Factory, Institute of Materials Structure Science, High Energy Accelerator Research Organization (KEK), 1-1 Oho, Tsukuba 305-0801, Japan.

[7] Institute of Physics, Academia Sinica, Taipei 11529, Taiwan

[8] Department of Physics, Northeastern University, Boston, Massachusetts 02115, USA

[9] Department of Applied Chemistry, Tokyo Institute of Technology, Tokyo 152-8552, Japan

*e-mail: yoshinori.okada@wpi-aimr.tohoku.ac.jp

We report the observation of coherent surface states on cubic perovskite oxide $SrVO_3$(001) thin films through spectroscopic-imaging scanning tunneling microscopy. A direct link between the observed quasiparticle interference patterns and the formation of a d_{xy}-derived surface state is supported by first-principles calculations. We show that the apical oxygens on the topmost VO_2 plane play a critical role in controlling the coherent surface state via modulating orbital state.

Establishing a microscopic understanding of the mechanism leading to coherent two-dimensional (2D) electronic states at surfaces/interfaces of transition metal perovskite oxides is a key step for further exploration of exotic quantum states in various systems [1-5]. Despite an extensive investigation of transition metal perovskite oxides using angle-resolved photoemission spectroscopy (ARPES) [6-10], the underlying microscopic mechanism that leads to the formation of coherent electronic 2D states has remained elusive. In this connection, unraveling the link between the emergence of coherent surface states and atomic reconstruction constitutes an important step forward. Scanning tunneling microscopy (STM) and scanning tunneling spectroscopy (STS) allow us to observe the surface interference pattern with well-defined wave vectors [11-14], and reveal the microscopic mechanism giving rise to coherent electronic 2D states. However, perovskite materials are intrinsically three-dimensional (3D) crystals, and obtaining atomically well-aligned surfaces has been difficult.

In this Letter, we report the first STM/STS observation of quasiparticle interference (QPI) patterns on the epitaxial film surfaces of perovskite oxide $SrVO_3$ (001). The $SrVO_3$ bulk has simple cubic symmetry with one electron in the 3d state, and hence it has been used as a prototype for understanding correlated transition metal perovskite oxides [15-29]. We interpret our experimental STM/STS results through parallel first-principles calculations to establish a microscopic understanding of the appearance and disappearance of the observed coherent surface states.

The epitaxial $SrVO_3$(001) thin films were grown on a buffered-HF-etched Nb-doped (0.05 wt.%) $SrTiO_3$(001) substrate by using pulsed laser deposition (PLD). In the three samples (thicknesses: 20, 40, and 110 nm) prepared for this study [30], the X-ray diffraction patterns showed negligible epitaxial strain. We used a scanning tunneling microscope equipped with PLD system to transfer the as-deposited thin films to a low-temperature (4 K) STM head under ultra-high vacuum conditions [45]. Figure 1(a) presents an STM topographic image of the $SrVO_3$(001) surface showing a square lattice of protrusions along with randomly distributed defects. The periodicity of the protrusions is approximately 5.5 Å and exhibits a ($\sqrt{2}\times\sqrt{2}$)-*R*45° surface reconstruction everywhere on the scanned surfaces.

The √2×√2 superlattice surface structure [Fig. 1(c)] is formed by a VO_2-terminated layer with apical oxygen adsorption [46,47]. Naively, we would expect the topmost V atoms to have similar valence as the bulk V^{4+} atoms because the bulk structure can be seen as stacked $(Sr^{2+}O^{2-})^0$ and $(V^{4+}O^{2-}{}_2)^0$ layers. However, previous emission-angle-dependent photoemission studies show more V^{5+} atoms on the surface [22, 48], which means that the V atoms near the surface are more oxidized than those in the bulk [49]. This observation excludes the possibility of a *bare* VO_2 termination with √2×√2 buckling near the surface since such a surface structure is unlikely to accommodate substantially oxidized V atoms. A 50% coverage of the apical oxygen sites (forming a $SrVO_{3.5}$ surface structure) is however allowed, which in turn would lead to the formation of the √2×√2 superlattice. Similar √2×√2 superstructures with 50% coverage of the apical oxygen sites have also been seen in manganite perovskites [50-52].

Figure 1(d) shows spatially-averaged differential conductance (dI/dV) spectra. The metallic electronic properties observed on the surface are consistent with previous photoemission experiments [20, 49]. The dI/dV spectra show a large spectral weight at zero sample bias voltage V_s, a peak at V_s = +400 mV, and two minima at V_s = −410 mV and +710 mV. Right at the peak position (V_s = +400 mV), a shoulder structure has also been observed in angle-integrated inverse photoemission experiments [53]. The energy at −410 mV for the conductance minimum agrees quantitatively with the band-edge position at the $\bar{\Gamma}$ point in previous ARPES studies [20].

Figures 2(a) and 2(b) show the topographic and differential conductance images which were simultaneously measured at V_s= −150 mV. In order to extract the QPI pattern, which is present only in the conductance image, we compared the Fourier transforms (FTs) of the two images in Figs. 2(c) and 2(d). While both FT images show peaks at √2×√2 spots [green circles in Fig. 2(c)], only the conductance FT image clearly exhibits an additional periodicity with respect to momentum [green dashed ellipses in Fig. 2(d)]. Figure 2(e) shows the energy-dependent intensity profile of the FT images along the $\overline{\Gamma X}$ direction for the three samples. The clear energy dispersion seen in Fig. 2(e) provides indisputable evidence for the existence of coherent electronic

states on the $SrVO_3$(001) surface. Hereafter, we will refer to this characteristic momentum dispersion along the $\overline{\Gamma X}$ direction as q^*.

In order to understand the energy dependence of the QPI pattern, we constructed a semi-infinite slab model using Wannier functions derived from first-principles density functional theory (DFT) (see Supplementary Materials for computational details [30]). We refer to an O-adsorbed V-atom site as "V_O-site" and to a bare V-atom site without apical oxygen as "V_b-site" [Fig. 3(a)]. Figure 3(b) shows the obtained orbital-dependent densities of states (DOSs) and the total DOS averaged over V_O and V_b sites [54]. Using a bandwidth renormalization factor of 0.4, which is close to the value obtained from previous ARPES experiments [20] and first principles calculations [21], the total surface DOS [bold black curve in Fig. 3(b)] captures the overall behavior of the experimental dI/dV spectrum [Fig. 1(d)] [55]. Such a renormalization of the DFT bands should reasonably describe the orbital information needed to model the emergent QPI pattern.

In order to establish that the QPI pattern is directly linked to the formation of the d_{xy}-derived coherent 2D band on the surface, we project the spectral weight of d_{xy}- and d_{xz}/d_{yz}- derived bands at V_O- and V_b-sites onto the surface Brillouin Zone (BZ) [Fig. 3(c)]. Results along the high-symmetry lines are shown in Figs. 3(d)-(g). For the V_O-site as well as the V_b- site, the d_{xy}-derived spectral weight shows a clear energy dispersion [Figs. 3(d,f)], indicating that the d_{xy}-derived bands feature a strong 2D character on the (001) surface. Importantly, at low energies, this d_{xy}-derived 2D spectral weight becomes the dominant electronic component at both V_O- and V_b- sites [see shaded region on the top horizontal axis in Fig. 3(b)], where a clear QPI pattern is observed. Furthermore, the interlayer coupling between the in-plane extended d_{xy} orbitals is small and their surface onsite energies are higher than the bulk [0.1eV and 0.3 eV higher for V_O- and V_b- sites, respectively, see Fig. 3(k)]. Therefore, we conclude that the emergent QPI pattern on the surface originates from d_{xy}-derived quasiparticle surface states, which are more or less isolated not only from the surface d_{xz}/d_{yz} states but also from the corresponding bulk states.

Our calculations also capture the appearance of the momentum q^* selectively along the $\overline{\Gamma X}$ direction. We computed the scattering probability $I(\boldsymbol{q})$ in terms of the spectral weight $A(\boldsymbol{k})$ using $I(\boldsymbol{q}) = \int A(\boldsymbol{k}) \times A(\boldsymbol{k}+\boldsymbol{q}) \mathrm{d}\boldsymbol{k}$. Typical $A(\boldsymbol{k})$ and $I(\boldsymbol{q})$ results using $E_{re} = -250$ meV are shown in Figs. 3(h) and 3(i). Because the shape of $A(\boldsymbol{k})$ deviates from a simple circle, the joint-DOS is significantly enhanced along the $\overline{\Gamma X}$ direction in $I(\boldsymbol{q})$. The magnitude and direction of this enhanced joint-DOS [Fig. 3(i)] is consistent with the q^* value obtained from the experimental conductance image at the corresponding energy eV_s= -250meV [Fig. 3(j)].

As the energy increases across the Fermi level E_F (here E_F is set to zero), the QPI signal gradually weakens in intensity and ultimately disappears altogether [Fig. 2(e)]. This fading of the QPI signal near E_F contradicts the behavior of simple metallic surfaces in which, according to conventional Fermi liquid theory, quasiparticle states would have a longer lifetime near E_F, and as a result, the QPI patterns would be more prominent [56]. We consider three possible scenarios in this connection: (1) Suppression (decoherence) of the quasiparticle interference via inelastic electron-electron, electron-phonon and/or electron-plasmon scatterings. However, the symmetric energy dependence on both sides of E_F expected for these inelastic scattering processes contradicts the monotonic fading of the QPI signal observed across E_F; (2) Effect of the shape of $A(\boldsymbol{k})$. This scenario however is also unlikely because the shape of the calculated $A(\boldsymbol{k})$ changes from circle-like (smaller joint-DOS) to square-like (larger joint-DOS) across E_F, which completely fails to explain the observed QPI signal fading; and (3) Suppression of the d_{xy}-derived spectral weight itself. Indeed, our numerical results show a suppression of the d_{xy}-derived spectral weight, especially at the V_b-site [dotted square in Fig. 3(f)]. This is driven by two mechanisms: (i) hybridization and (ii) sublattice formation.

The first mechanism, which involves hybridization between the d_{xy}- and d_{xz}/d_{yz}- derived states at the V_b-site, is illustrated schematically in Fig. 4(a) [57]. As the axially-extended d_{xz}/d_{yz}-derived *bulk* bands have an intrinsically strong dispersion normal to the (001) surface, the projection of these bands onto the (001) surface BZ results in a broad spectral weight distribution in momentum space. The broad distribution of the spectral weight at the V_b-site [Fig. 3(g)] indicates the existence of a strong coupling between the d_{xz}/d_{yz}-derived *surface* and *bulk* bands. Such a strong mixing can be naturally understood from the smaller bulk-surface

energy separation (~0.2 eV) for d_{xz}/d_{yz} orbital at the V_b-site compared to that for the Vo-site (~1.2 eV) [Fig. 3(k)]. An important consequence is the possible coexistence of the d_{xy}- and d_{xz}/d_{yz}- derived bands at the same energy (E) and momentum (k) over a wide range across the Fermi level [dotted square in Fig. 3(f)]. The hybridization with the d_{xz}/d_{yz}-derived bands then leads to (i) the suppression of the d_{xy}-derived spectral weight through spectral weight transfer, and (ii) the enhancement of the scattering channel between d_{xy}- and d_{xz}/d_{yz}-derived states at the V_b site.

We next discuss the mechanism of sublattice formation, which involves transfer of the spectral weight from the d_{xy} orbital at the V_b-site to the d_{xy} orbital at the V_O-site, as shown schematically in Fig. 4(b). The calculated on-site energies for the d_{xy} orbital at the V_O- and V_b- sites are ~0.1 and ~0.3 eV, respectively. In general, a difference in on-site energies will induce a spectral weight transfer between these inequivalent sites around the zone boundary [58]. We confirm this effect by focusing on the d_{xy}-derived lower energy-band branch near the $\bar{X}$ point [dotted squares in Figs. 3(d) and 3(f)]. Our numerical results show that around the $\bar{X}$ point, the d_{xy}-state spectral weight at the V_b site (with higher potential) is more suppressed compared to the d_{xy}-state spectral weight at the V_O-site (with lower potential) around the same (E, k) region.

The preceding discussion of hybridization and sublattice formation mechanisms suggests that it is the non-uniformity of the d_{xy}-derived spectral weight [Fig. 4(c)] that principally causes the QPI signal on the ($\sqrt{2}\times\sqrt{2}$)-$R45^o$ surface to fade monotonically with energy. At low energies, we obtain a rather uniform distribution of the d_{xy}-derived spectral weight [see Fig. 4(d)]. In contrast, at higher energies, this spectral weight is suppressed while inter-orbital scatterings are enhanced at the V_b-site [see Fig. 4(c)]. Both mechanisms act to disrupt the uniformity of the d_{xy}-derived spectral weight [see also Fig. S6].

Our results provide important insights for designing 2D quasiparticle states at surfaces/interfaces of perovskite oxides. We identify the pivotal role of apical oxygens in the formation of 2D electronic states via orbital modulation. Because of the large onsite energy difference at the V_O-site, the negatively-charged apical oxygen strongly eliminates electrons selectively from the axially-extended d_{xz} and d_{yz} states [see Fig. 3(k) (left)]. The

apical oxygen thus plays a key role in isolating the in-plane d_{xy} and out-of-the-plane d_{xz}/d_{yz} orbitals on the (001) surface. Since apical oxygens are ubiquitous in perovskite oxides, these considerations would also be relevant for designing systems such as the cuprates, where the interplay between the d_{x2-y2} and out-of-the-plane orbitals including d_{z2} is important [59], as well as for surfaces/interfaces involving sublattice formation more generally. We should keep in mind, however, that an obvious unique factor in $SrVO_3$ is its electron filling of one electron in the *bulk* 3d system. Interestingly, our results suggest that the $SrVO_3$(001) surface is similar to the 2D metallic state at $SrTiO_3$(001)-based surfaces/interfaces because in both systems the degeneracy of the t_{2g} orbitals is lifted and the d_{xy}-derived band becomes dominant at low energies [60-72]. This similarity points out that the $SrVO_3$(001) surface would be an interesting playground for exploring emergent quantum functionalities such as magnetism and superconductivity.

We thank H. Ishida, and K. Sato for helpful discussions, and D. Walkup and P. Han for critical reading of the manuscript. Y. O. acknowledges funding from the Japan Society for the Promotion of Science grant-in-aid numbers 26707016 and 25886004. T. H. acknowledges funding from the Japan Society for the Promotion of Science grant-in-aid numbers 26246022, 26106502, JST-CREST, and JST-PRESTO. This work was supported by the World Premier Research Center Initiative, promoted by the Ministry of Education, Culture, Sports, Science and Technology of Japan. The work at Northeastern University was supported by the US Department of Energy (DOE), Office of Science, Basic Energy Sciences grant number DE-FG02-07ER46352 (core research), and benefited from Northeastern University's Advanced Scientific Computation Center (ASCC), the NERSC supercomputing center through DOE grant number DE-AC02-05CH11231, and support (applications to layered materials) from the DOE EFRC: Center for the Computational Design of Functional Layered Materials (CCDM) under DE-SC0012575. H. L. acknowledges the Singapore National Research Foundation for support under NRF award number NRF-NRFF2013-03.

References

[1] H. Y. Hwang, *et al.*, *Nature Mater.* **11**, 103 (2012).

[2] A. Ohtomo, D. A. Muller, J. L. Grazul, and H. Y. Hwang, *Nature* **419,** 378–380 (2002).

[3] A. Ohtomo, and H. Y. Hwang, *Nature* **427,** 423–426 (2004).

[4] Y. Xie, C. Bell, M. Kim, H. Inoue, Y. Hikita, and H. Y. Hwang, *Solid State Commun.* **197**, 25 (2014).

[5] Y. Z. Chen, *et al*., *Nature Mater.* **14,** 801-806 (2015).

[6] T. Yoshida, *et al*., *Phys. Rev. Lett.* **95,** 146404 (2005).

[7] A. F. Santander-Syro, *et al., Nature* **469,** 189-193 (2011).

[8] W. Meevasana, *et al*., *Nature Mater.* **10,** 114–118 (2011).

[9] K. Yoshimatsu, *et al*., *Science* **333,** 319-322 (2011).

[10] P. D. C. King, *et al.*, *Nat. Commun.* **5**, 3414 (2013).

[11] M. Crommie, C. P. Lutz, and D. M. Eigler, *Nature* **363,** 524–527 (1993).

[12] Y. Hasegawa, and Ph. Avouriw, *Phys. Rev. Lett.* **71,** 1071 (1993).

[13] J. E. Hoffman, *et al., Science* **297,** 1148–1151 (2002).

[14] J. Lee, *et al., Nature Phys.* **5,** 800–804 (2009).

[15] H. Eskes, M. B. J. Meinders and G. A. Sawatzky, *Phys. Rev. Lett.* **67,** 1035 (1991).

[16] A. Fujimori, *et al.*, *Phys. Rev. Lett.* **69** 1796 (1992).

[17] E. Pavarini, A. Yamasaki, J. Nuss, and O. K. Andersen, *New J. Phys.* **7,** 188 (2005).

[18] A. Liebsch, *Phys. Rev. Lett.* **90** 096401 (2003).

[19] H. Ishida, D. Wortmann, and A. Liebsch, *Phys. Rev. B* **73**, 245421 (2006).

[20] M. Takizawa, *et al.*, *Phys. Rev. B* **80**, 235104 (2009).

[21] See, for example, I. A. Nekrasov *et al.*, Phys. Rev. B **73**, 155112 (2006), C. Taranto *et al.*, Phys. Rev. B 88, 165119 (2013), and J. M. Tomczak, *et al.*, Phys. Rev. B 90, 165138 (2014).

[22] M. Takizawa, *et al.*, *arXiv*:0806.2231.

[23] S. Aizaki, *et al*., *Phys. Rev. Lett.* **109,** 056401 (2012).

[24] M. Kobayashi, *et al.*, *Phys. Rev. Lett.* **115,** 076801 (2015).

[25] T. Yoshida, *et al.*, *J. Electron. Spectrosc. Relat. Phenom.* **208**, 11 (2016).

[26] S. Backes, *et al.*, *Phys. Rev. B* **94**, 241110 (2016).

[27] Z. Zhong, *et al.*, *Phys. Rev. Lett.* **114**, 246401 (2015).

[28] V. Pardo, and W. E. Pickett, *Phys. Rev. B* **81**, 245117 (2010).

[29] U. Lüders, W. C. Sheets, A. David, W. Prellier, and R. Frésard, *Phys. Rev. B* **80**, 241102 (2009).

[30] See Supplemental Material, which includes Refs. [20,31-45], at https://journals.aps.org/prl/abstract/***/PhysRevLett.***#supplemental for details of film growth conditions and characterizations, and theoretical calculations.

[31] P. Dougier, J. C. C. Fan, and J. B. Goodenough, *J Solid State Chem*. **14,** 247-259 (1975).

[32] M. J. Rey, *et al*. *J. Solid State Chem.* **86,** 101 (1990).

[33] M. Onoda, *et al.*, *Solid State Commun.* **79,** 281 (1991).

[34] S. Phark, *et al.*, *Appl. Phys. Lett.* **98,** 161908 (2011).

[35] M. Gu, S. A. Wolf, and J. Lu, *arXiv*:1307.5819.

[36] J. A. Moyer, C. Eaton, and R. E. Herbert, *Adv. Mater.* **25,** 3578 (2013).

[37] J. P. Perdew, K. Burke, and M. Ernzerhof, *Phys. Rev. Lett.* **77,** 3865 (1996).

[38] P. E. Blöhl, *Phys. Rev. B* **50,** 17953 (1994).

[39] G. Kresse and J. Furthmüler, *Comput. Mater. Sc.* **6,** 15 (1996).

[40] Y. C. Lan, X. L. Chen, and M. He, *J. Alloys Compd.* **354,** 95–98 (2003).

[41] N. Marzari and D. Vanderbilt, *Phys. Rev. B* **56,** 12847 (1997).

[42] I. Souza, N. Marzari, and D. Vanderbilt, D. *Phys. Rev. B* **65,** 035109 (2001).

[43] A. A. Mostofi, *et al*. *Comput. Phys. Commun.* **178,** 685 (2008).

[44] C. Franchini, *J. Phys.: Condens. Matter* **24,** 235602 (2012).

[45] K. Iwaya, R. Shimizu, T. Hashizume, and T. Hitosugi, *Rev. Sci. Instrum.* **82,** 083702 (2011).

[46] A buffered-HF-etched step-and-terrace $SrTiO_3$ substrate terminates with TiO_x. Accordingly, SrO and VO_2 layers are stacked alternately starting with the SrO layer to form SrO–TiO_2–SrO–VO_2 structures at the substrate/film interface. Therefore, after deposition the topmost layer, which contains cations, is VO_2.

[47] Since more oxygen is available in the $Sr_2V_2O_7$ target compared with that in $SrVO_3$, additional oxygen can be adsorbed on the topmost VO_2 layer during film growth in ultra-high vacuum (see [30]).

[48] We employed the same film growth conditions as in previous studies [9, 20, 22, 23, 24], including the chemical composition of the target material $Sr_2V_2O_7$ used for film growth. In these studies, the ($\sqrt{2}\times\sqrt{2}$)-*R*45°

structure on the surface was also seen with LEED. Our angle-dependent photoemission data (not shown) indicates that the intensity for V increases relative to that of Sr in more surface sensitive photoelectron detection angles. This fact supports the $VO_{2.5}$–termination scenario, as shown in Figs. 1(b) and (c).

[49] Valence of the topmost V has more 5+ component, as compared to the bulk value of 4+. Note that the topmost V state is not equal to 5+.

[50] J. X. Ma, *et al., Phys. Rev. Lett.* **95**, 237210 (2005).

[51] K. Fuchigami, *et al., Phys. Rev. Lett.* **102**, 066104 (2009).

[52] Z. Gai *et al., Nature Communications* **5**, 4528 (2013).

[53] K. Morikawa, *et al*., *Phys. Rev. B* **52,** 13711 (1995).

[54] We increased the electron filling on the pristine surface in our computation by raising the chemical potential to match the experimentally observed QPI dispersion. The origin of this electron doping to surface can be due to extra missing apical oxygens on $\sqrt{2}\times\sqrt{2}$ sub-lattice [see dark spots in Fig. 1(a)]. The density of these apical oxygen defects is at most 0.2 per V-site.

[55] Formation of the conductance minimum at V_s = -410 mV can be explained by the combined effects of the enhanced conductance of 3d states peaking at +400 meV, and the tail of the enhanced conductance due to incoherent spectral weight and/or oxygen 2p state, which peaks well below -1 eV. While the overall experimental dI/dV curve [Fig. 1(d)] is reasonably described by our calculated total DOS [Fig. 3(b)], the DOS also features additional peaks which do not appear in the dI/dV curve. These extra peaks could be washed out by a number of effects that are not included in our modeling of the dI/dV , such as the effects of the tunneling matrix element, complications due to the tip DOS, and the broadening of electronic states due to finite lifetime and other effects.

[56] L. Bürgi, O. Jeandupeux, H. Brune, and K. Kern, *Phys. Rev. Lett.* **82,** 4516 (1999).

[57] Since the surface structure is not a cubic Pm3m space group, the d_{xy} and d_{yz} orbitals are not orthogonal on the surface, and hence are allowed to hybridize.

[58] Kittel, C. *Introduction to Solid State Physics*, *Wiley*. 8th edition (2005).

[59] E. Pavarini, *et al*., Phys. Rev. Lett. 87, 047003 (2001).

[60] S. Thiel, *et. al.*, *Science* **313,** 1942 (2006).

[61] J. A. Sulpizio, S. Ilani, P. Irvin, and J. Levy, *Annu. Rev. Mater. Res.* **44,** 117 (2014).

[62] S. Thiel, G. Hammerl, A. Schmehl, C. W. Schneider, and J. Mannhart, *Science* **313,** 1942 (2006).

[63] J. Son, *et al*. *Nature Mater.* **9,** 482 (2010).

[64] H. Ohta, *et al.*, *Nature Mater.* **6**, 129 (2007).

[65] A. D. Caviglia, *et al*. *Nature* **456,** 624 (2008).

[66] Y. Kozuka, *Nature* **462,** 487 (2009).

[67] K. Ueno, *et al*., *Nature Mater.* **7,** 855 (2008).

[68] A. Brinkman, *et al*., *Nature Mater.* **6,** 493 (2007).

[69] J. A. Bert, *et al*., *Nature Phys.* **7,** 767 (2011).

[70] L. Li, C. Richter, J. Mannhart, and R. C. Ashoori, *Nature Phys.* **7,** 762 (2011).

[71] H. W. Jang, *et al*., *Science* **331,** 886 (2011).

[72] M. S. Scheurer, and J. Schmalian, *Nature Commun.* **6**, 6005 (2014).

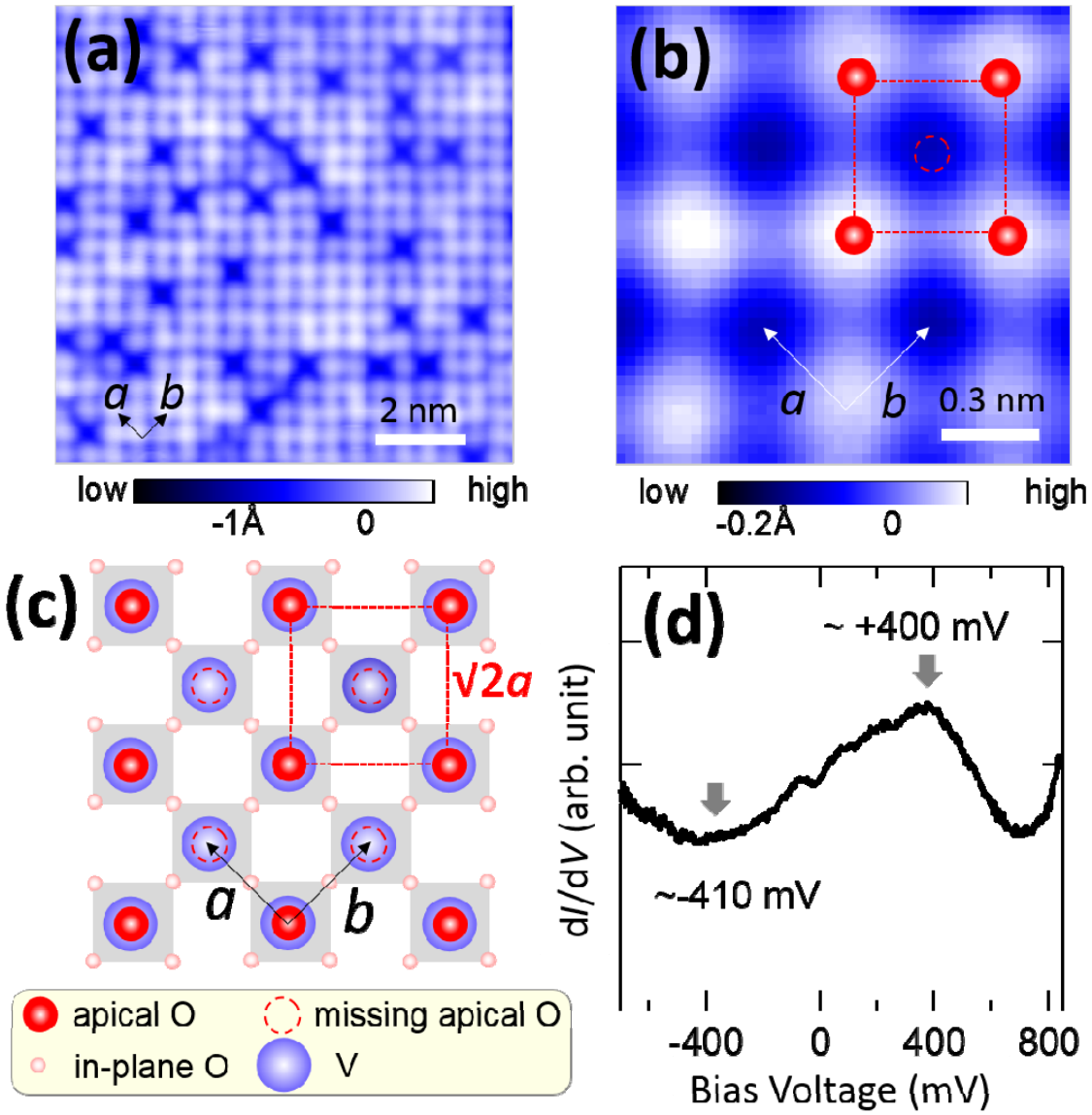

FIG. 1 (color online) Typical topographic images of $SrVO_3$(001) surface and metallic tunneling spectra (110-nm-thick film)**. (a), (b)** Topographic images with sample bias voltage $V_s = -100$ mV **(a)**; the enlarged image in **(b)** shows the (√2×√2)-*R*45° structure. **(c)** The model used to generate the topographic image with a (√2×√2)-*R*45° structure. **(d)** Spatially-averaged tunneling spectra (d*I*/d*V*) obtained from the surface.

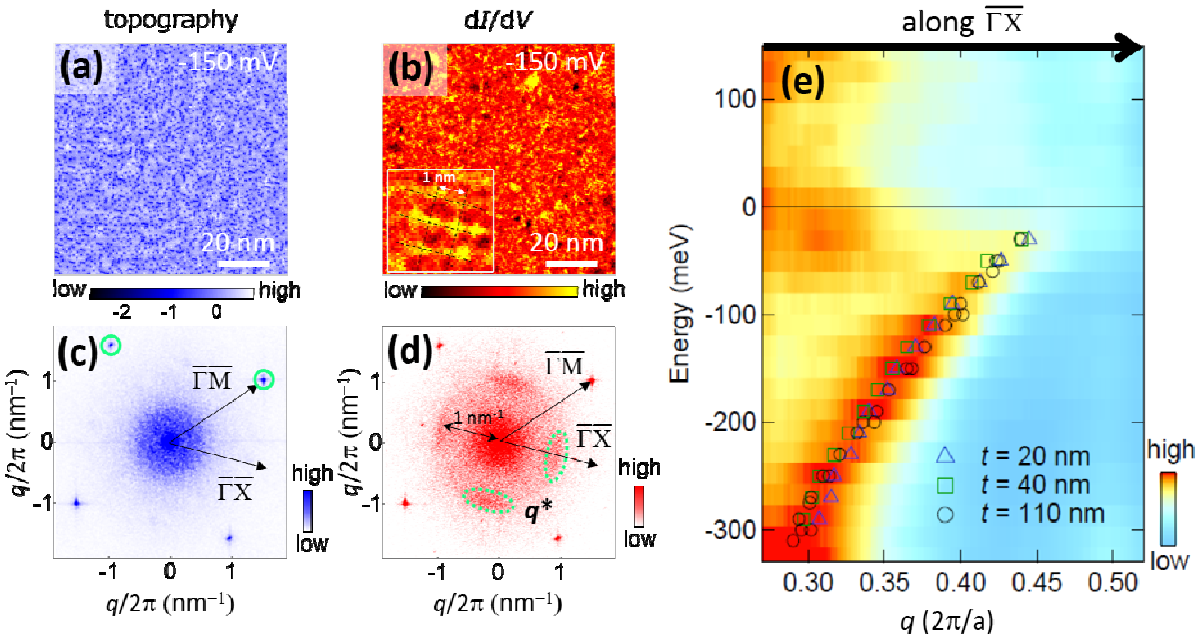

FIG. 2 (color online) Observation of quasiparticle interference (QPI) pattern on the surface of $SrVO_3$(001). **(a), (b)** Simultaneously acquired topographic **(a)** and conductance **(b)** images at $V_s = -150$ mV. The inset in **(b)** shows the enlarged image in which we can see a wave-like pattern with approximately 1 nm periodicity. **(c)**, **(d)** FTs of **(a)** and **(b)**, respectively. Bragg peaks representing the $\sqrt{2}a \times \sqrt{2}a$ apical oxygen structure are highlighted by green circles in (c), and the wave-vector $\boldsymbol{q}^*$ is highlighted by green-dashed ellipses in **(d)**. $\overline{\Gamma X}$ direction corresponds to the direction of the nearest-neighbor V atoms. The data shown in **(a)**-**(d)** are taken from a 110-nm-thick film. **(e)** Energy-dependent intensity profiles of the FTs along $\overline{\Gamma X}$ (intensity averaged over three samples with thickness 20 nm, 40nm, and 110 nm), along with the values of q^* obtained from the three films. QPI patterns were independent of film thickness (Fig. S2), which is consistent with fully relaxed films.

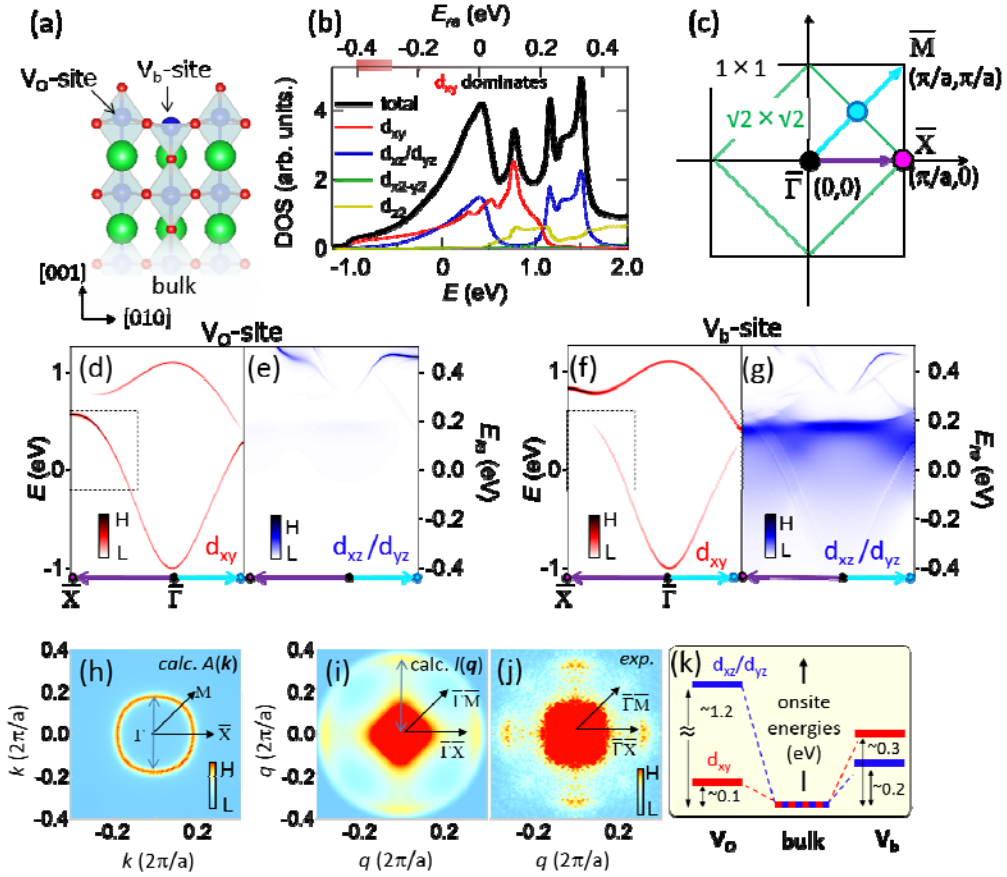

FIG. 3 (color online) Simulation of the electronic states on the surface of $SrVO_3$(001). **(a)** Cross-sectional view of the calculated relaxed near surface structure. V_O and V_b denote the V-atom sites with and without apical oxygen, respectively. (**b)** Calculated density of states averaged over V_O- and V_b-sites. (**c)** Schematic drawing of the surface Brillouin Zone (BZ). Green lines mark the BZ of ($\sqrt{2}\times\sqrt{2}$)-*R*45° structure. (**d)–(g)** Spectral weights of the d_{xy} and d_{xz}/d_{yz} orbitals for V_O (V_b) are shown in **(d)** and (**e**) ((**f**) and (**g**)), respectively. The top axis of (**b**) and right axes of (**d)–(g)** represent *renormalized* energy scale E_{re} using a renormalization factor of 0.4 (*i.e.*, $E_{re} = 0.4E$). **(h)-(j)** Simulated total spectral weight at $E_{re} = -250$ mV (**h**) and the associated scattering probability (**i**). The experimental Fourier transform image of conductance mapping at V_s=-250 mV is shown in (**j**) for comparison with (**i**). (**k**) The orbital- and site-dependence of onsite energies relative to the degenerate bulk t_{2g} states; see Table S2 for details. The onsite energy differences within our model mainly reflect local crystal field effects; these are not related to onsite Coulomb repulsion *U*. See [30] for details of our calculations.

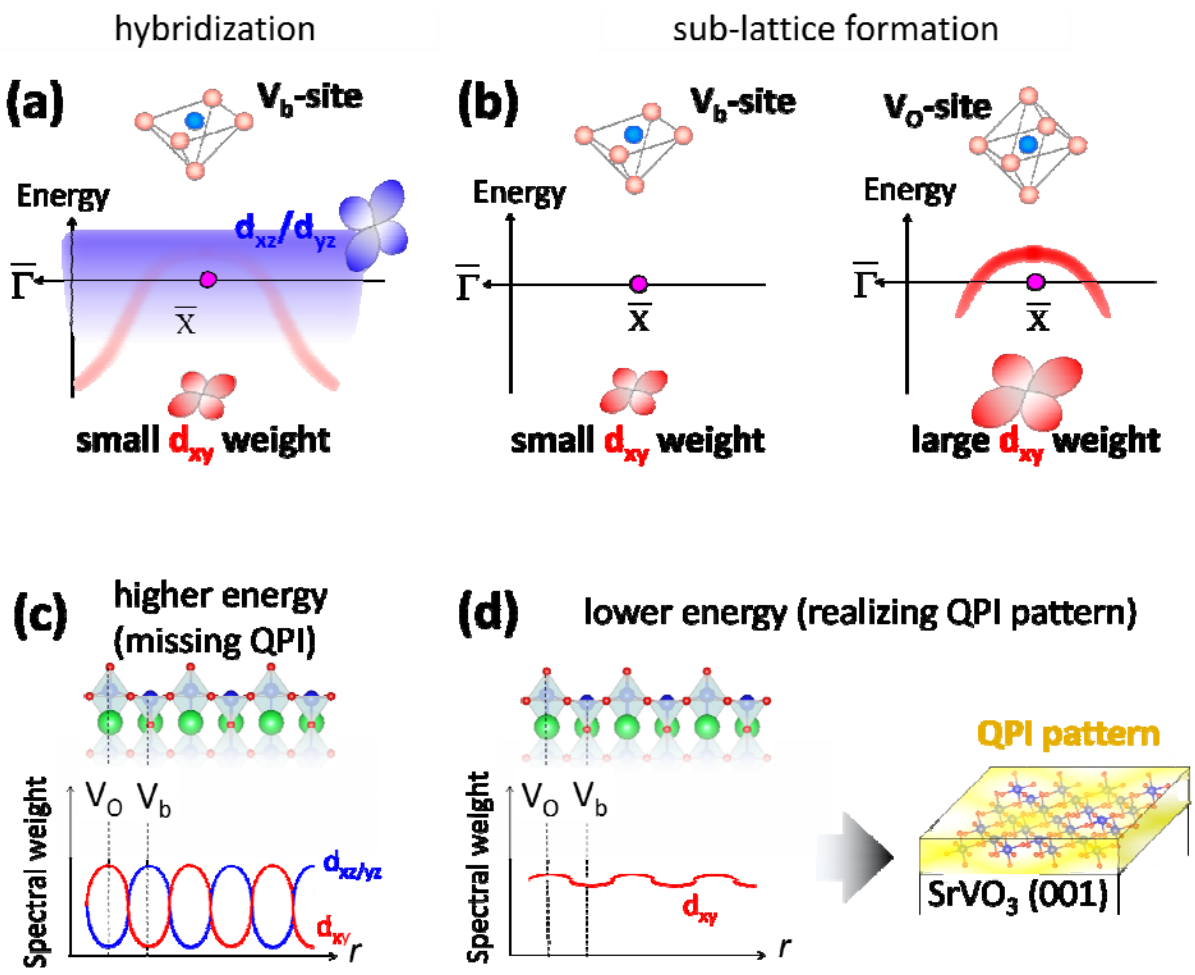

FIG. 4 (color online) Schematic illustration of inter-orbital and intra-orbital spectral weight transfer mechanisms and the related appearance/disappearance of QPI patterns. **(a)** Spectral weight transfer from d_{xy} orbitals (red) to d_{xz}/d_{yz} orbitals (blue) at the V_b-site. (**b)** Spectral weight transfer from d_{xy} orbitals (red) at the V_b-site (left) to d_{xy} orbitals (red) at the V_O-site (right). (**a**) and (**b**) only highlight the lower energy band branch near the $\bar{X}$ point. (**c**), (**d)** Distribution of d_{xy}- and d_{xz}/d_{yz}- derived spectral weight in real space for high (**c**) and low (**d**) energy regions.